A Spectral Scheme to Simulate Dynamic Fracture Problems in Composites

Changyu Hwang[1], **Philippe H. Geubelle**[2]

Abstract: This paper presents the formulation and numerical implementation of a spectral scheme specially developed to simulate dynamic fracture events in unidirectional and cross-ply fiber-reinforced composites. The formulation is based on the spectral representation of the transversely isotropic elastodynamic relations between the traction stresses along the fracture plane and the resulting displacements. Example problems involving stationary or dynamically propagating cracks in fiber-reinforced composites are investigated and compared with reference solutions available in the literature and/or experimental observations.

keyword: Spectral method, transversely isotropic solid, fiber-reinforced composites, dynamic fracture.

1 Introduction

The relatively weak resistance of composite materials to dynamic loading has long constituted a major obstacle to their wider use in a variety of engineering applications. The most notorious example of dynamic failure of composite structures is undoubtedly the extensively studied impact-induced delamination (Abrate, 1998), in which substantial subsurface damage can take place in a composite laminate without apparent subsurface damage in the vicinity of the impact point. Simulations of the complex failure process associated with impact-induced delamination of thin composite plates have indicated the very rapid propagation of planar failure surfaces at the interface between adjacent plies (Geubelle and Baylor, 1998). Rapid propagation of planar cracks has also been observed in thicker uni- and multidirectional composites (Chai, Knauss and Babcock, 1983; Lambros and Rosakis, 1997ab), including the appearance of intersonic crack speeds under shear-dominated loading conditions (Coker and Rosakis, 1998). This phenomenon is reminiscent of that observed in homogeneous isotropic systems, and is further discussed in Section 4.

These various observations have motivated the present development of an efficient numerical scheme able to investigate in great details a wide range of fundamental dynamic fracture problems involving a planar crack embedded in an infinite linearly elastic unidirectional or cross-ply composite medium and subjected to any quasi-static or dynamic loading conditions. The spectral form of the boundary integral formulation presented in this paper is directly inspired from previous developments of the numerical scheme used in the analysis of 2D and 3D fundamental dynamic fracture problems in homogeneous (Geubelle and Rice, 1995) and bimaterial (Geubelle and Breitenfeld, 1997; Breitenfeld and Geubelle, 1998) media. The spectral formulation relies on the elastodynamic relations, expressed in the Fourier domain, between the traction stresses acting along the fracture plane and the associated displacement and velocity components. The numerical scheme allows for the introduction of almost any type of cohesive failure law for the simulation of spontaneous crack initiation, propagation and arrest. A wide range of friction models can also be incorporated to capture the possible contact between the crack faces.

The paper is organized as follows: in Section 2, we start with a brief review of the elastodynamic relations for a transversely isotropic material, then summarize the derivation of the corresponding 2D spectral formulation and implementation. In Section 3, we show how the spectral scheme can be used to solve the problem of a stationary crack subjected to a sudden uniform mixed-mode loading. Special emphasis is placed there on the accurate capture of the complex wave patterns and on the extraction of the time-dependent stress intensity factors characterizing the near-tip fields. Section 4 is dedicated to the simulation of subsonic and intersonic crack propagation in unidirectional and cross-ply composite media and to a comparison with the experimental observations obtained by Coker and Rosakis (1998).

2 Transversely isotropic spectral formulation

The spectral formulation developed hereafter aims at the accurate and efficient solution of three types of 2D dynamic fracture problems in fiber-reinforced composite media. The first two types are concerned with the dynamic failure of unidirectional composites, for which the symmetry axis (i.e., the fiber direction) is either perpendicular (Fig. 1a) or parallel (Fig. 1b) to the crack front. Defining a reference Cartesian coordinate system with the x_2-axis perpendicular to the fracture plane and the x_3-axis parallel to the crack front, these first two problems are referred to as the 0° and 90° cases, respectively. The third type of fracture problem considered in this paper is associated with the dynamic delamination of a [0/90] cross-ply composite (Fig. 1c), with the planar crack propagating along the planar interface. In addition to the two-dimensionality of the dis-

[1] Center for Simulation of Advanced Rockets

[2] Center for Simulation of Advanced Rockets, Department of Aeronautical and Astronautical Engineering, Univ. of Illinois, Urbana-Champaign, IL, USA.

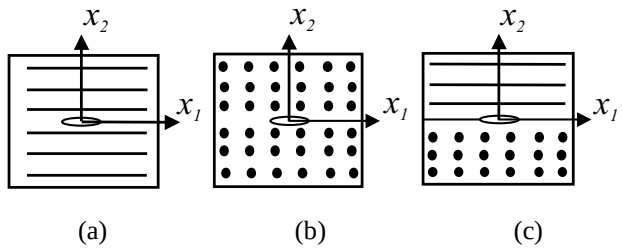

Figure 1 : Fiber-reinforced composites; (a) fibers in x_1-direction, (b) fibers in x_3-direction, (c) bimaterial system.

placement, $u_i(x_1, x_2, t)$ and stress $\sigma_{ij}(x_1, x_2, t)$ fields, we further assume that the dynamic response and failure of the composite is adequately captured by the homogenized anisotropic elasticity theory, thereby neglecting the heterogeneity associated with the multi-phase microstructure.

We start the derivation of the spectral formulation from the displacement form of the elastodynamic relations, which, for the two special fiber orientations considered here, take a simpler form allowing for the decoupling of the in-plane and out-of-plane motions. For the 0° case, the in-plane motion is described by

$$c_{11}\frac{\partial^2 u_1}{\partial x_1^2} + c_{66}\frac{\partial^2 u_1}{\partial x_2^2} + (c_{12}+c_{66})\frac{\partial^2 u_2}{\partial x_1 \partial x_2} = \rho\frac{\partial^2 u_1}{\partial t^2}, \tag{1}$$

$$c_{66}\frac{\partial^2 u_2}{\partial x_1^2} + c_{22}\frac{\partial^2 u_2}{\partial x_2^2} + (c_{12}+c_{66})\frac{\partial^2 u_1}{\partial x_1 \partial x_2} = \rho\frac{\partial^2 u_2}{\partial t^2}, \tag{2}$$

and the out-of-plane motion by

$$c_{66}\frac{\partial^2 u_3}{\partial x_1^2} + \frac{1}{2}(c_{22}-c_{23})\frac{\partial^2 u_3}{\partial x_2^2} = \rho\frac{\partial^2 u_3}{\partial t^2} \tag{3}$$

The five elastic constants c_{11} , c_{22} , c_{12} , c_{23} and c_{66} entering Eq. 1-3 define the constitutive relations for an isotropic medium with its symmetry axis aligned with the x_1 -axis:

$$\begin{Bmatrix} \sigma_{11} \\ \sigma_{22} \\ \sigma_{33} \\ \sigma_{23} \\ \sigma_{13} \\ \sigma_{12} \end{Bmatrix} = \begin{bmatrix} c_{11} & c_{12} & c_{12} & 0 & 0 & 0 \\ c_{12} & c_{22} & c_{23} & 0 & 0 & 0 \\ c_{12} & c_{23} & c_{22} & 0 & 0 & 0 \\ 0 & 0 & 0 & \frac{c_{22}-c_{23}}{2} & 0 & 0 \\ 0 & 0 & 0 & 0 & c_{66} & 0 \\ 0 & 0 & 0 & 0 & 0 & c_{66} \end{bmatrix} \times \begin{Bmatrix} \varepsilon_{11} \\ \varepsilon_{22} \\ \varepsilon_{33} \\ 2\varepsilon_{23} \\ 2\varepsilon_{13} \\ 2\varepsilon_{12} \end{Bmatrix} \tag{4}$$

For an isotropic solid, these elastic constants can be expressed in terms of the Lamé constants λ and μ as

$$c_{11} = c_{22} = \lambda + 2\mu, \quad c_{12} = c_{23} = \lambda, \text{ and } c_{66} = \mu \tag{5}$$

The elastodynamic relations associated with the 90° case are similar and are listed in Appendix A. Transversely isotropic materials are characterized by three fundamental bulk wave speeds: the shear wave speed, c_s , the dilatational wave speed in the fiber direction, $c_d^{(1)}$, and the dilatational wave speed normal to fibers, $c_d^{(2)}$, respectively defined as

$$c_s = \sqrt{\frac{c_{66}}{\rho}}, \quad c_d^{(1)} = \sqrt{\frac{c_{11}}{\rho}}, \quad c_d^{(2)} = \sqrt{\frac{c_{22}}{\rho}}, \tag{6}$$

where ρ denotes the density of the material.

The basic steps leading to the derivation of the spectral formulation for a transversely isotropic material are somewhat similar to those used by Breitenfeld and Geubelle (1998) in the bimaterial isotropic case. Only the important relations corresponding to the 0° case are indicated here, with the main derivation steps summarized in Appendix B. The spectral formulation corresponding to the 90° case is summarized in Appendix D. The particular form of the spectral formulation used here is the so-called *independent formulation* introduced by Geubelle and Breitenfeld (1997), which has been shown to have better accuracy and stability than the original *combined formulation* presented by Geubelle and Rice (1995) under shear or mixed-mode loading conditions. It expresses the dynamic response of the two adjoining half spaces in two independent integral relations between the traction stresses and the boundary displacements, before joining the two elastodynamic solutions through appropriate interface conditions.

Let $\tau_i(x_1, t) = \sigma_{i2}(x_1, x_2 = 0, t)$ denote the dynamic traction stresses acting on the fracture plane $x_2 = 0$, and $u_i^{\pm}(x_1, t) = u_i(x_1, x_2 = 0^{\pm}, t)$ the boundary displacements. The fundamental form of the elastodynamic equations used in this work is

$$\tau_i(x_1, t) = \tau_i^0(x_1, t) \mp V_{ik}^{\pm}\frac{\partial u_k^{\pm}(x_1, t)}{\partial t} + f_i^{\pm}(x_1, t) \tag{7}$$

where $\tau_i^o(x_1, t)$ denotes the externally applied traction stress that would exist on the fracture plane if no crack was present; the second term, often referred to as the radiation term, corresponds to the instantaneous response of the material; the last term incorporates the dynamic effects associated with the non-uniform motion of the fracture surfaces. The superscripts "+" and "-" indicate quantities associated with the upper and lower materials, respectively, and are omitted unless required for clarity. In (7), V_{ij} denote the components of a diagonal matrix containing material properties

$$V_{11} = \frac{c_{66}}{c_s}, \quad V_{22} = \frac{c_d^{(2)}}{c_s^2}c_{66}, \quad V_{33} = \frac{c_{66}}{\beta c_s}, \tag{8}$$

where $\beta = \sqrt{2c_{66}/(c_{22}-c_{23})}$ ($\beta = 1$ for isotropic media). The last term in Eq. 7, $f_i(x_1, t)$, is the convolution term and

is expressed in the spectral domain as a time convolution between its Fourier coefficients $F_i(t;q)$ and the Fourier coefficients $U_i^{\pm}(t;q)$ of the boundary displacements $u_i^{\pm}(x_1,t)$ as

$$F_1^{\pm}(t;q) = \pm c_{66}^{\pm}|q| \int_0^t H_{11}\left(|q|c_s^{\pm}t'\right) U_1^{\pm}\left(t-t';q\right)|q|c_s^{\pm}dt'$$
$$+ ic_{66}^{\pm}|q| \left(2 - \frac{2+\eta^{(2)\pm}+\eta^{(3)\pm 2}}{1+\eta^{(2)\pm}}\right) U_2^{\pm}(t;q)$$
$$+ ic_{66}^{\pm}|q| \int_0^t H_{12}\left(|q|c_s^{\pm}t'\right) U_2^{\pm}(t-t';q)|q|c_s^{\pm}dt', \qquad (9)$$

$$F_2^{\pm}(t;q) = \mp c_{66}^{\pm}|q| \int_0^t H_{22}\left(|q|c_s^{\pm}t'\right) U_2^{\pm}\left(t-t';q\right)|q|c_s^{\pm}dt'$$
$$- ic_{66}^{\pm}|q| \left(2 - \frac{2+\eta^{(2)\pm}+\eta^{(3)\pm 2}}{1+\eta^{(2)\pm}}\right) U_1^{\pm}(t;q)$$
$$- ic_{66}^{\pm}|q| \int_0^t H_{12}\left(|q|c_s^{\pm}t'\right) U_1^{\pm}(t-t';q)|q|c_s^{\pm}dt', \qquad (10)$$

$$F_3^{\pm}(t;q) = \mp \frac{c_{66}^{\pm}}{\beta^{\pm}}|q| \int_0^t H_{33}\left(|q|c_s^{\pm}t'\right) U_3^{\pm}(t-t';q)|q|c_s^{\pm}dt' \qquad (11)$$

where q is the spectral mode number; i is the imaginary number; $\eta^{(1)} = \sqrt{c_{11}/c_{66}}$; $\eta^{(2)} = \sqrt{c_{22}/c_{66}}$; $\eta^{(3)} = \sqrt{c_{12}/c_{66}}$.

One of the major advantages of the spectral method is associated with the non-singular character of the convolution kernels H_{ij} entering (9-11). The convolution kernel for the out-of-plane motion, H_{33} , is identical to that entering the isotropic problem, and is given by $H_{33}(T) = J_1(T)/T$, where $J_1(T)$ denotes the Bessel function of the first kind. The expression of the convolution kernels $H_{\alpha\beta}$ for the in-plane motion is given in Appendix C. The convolution kernels are illustrated in Fig. 2 for a Graphite/Epoxy composite material with $c_{11} = 82\ GPa$, $c_{22} = 11.1\ GPa$, $c_{12} = 4.0\ GPa$, $c_{23} = 4.9\ GPa$ and $c_{66} = 3.6\ GPa$. As apparent in Fig. 2, the convolution kernels are non-singular, oscillating and decaying functions, and do not therefore require the special treatment associated with the (hyper)singular kernels encountered in more conventional boundary integral formulations.

To complete the spectral formulation Eq. 7-11, three components are needed. Firstly, appropriate interface conditions must be incorporated to link the elastodynamic solutions of the two half spaces described by Eq. 7. Four interface conditions must be considered: 1) the non-failing region, in which the traction stresses and displacements are continuous across the interface; 2) the cohesive failure zone, where the traction stresses are equal to the (possibly decaying) strength of the material; 3) the traction-free crack region, in which the traction stresses are set to zero; and 4) the possibility of spontaneous contact between the crack faces, where the interface conditions correspond to the continuity of the normal tractions and the absence of material interpenetration. See Section 3 in Breitenfeld and Geubelle (1998) for the implementation of the interface conditions. Secondly, a time stepping scheme must be introduced to integrate over time the velocity distribution derived

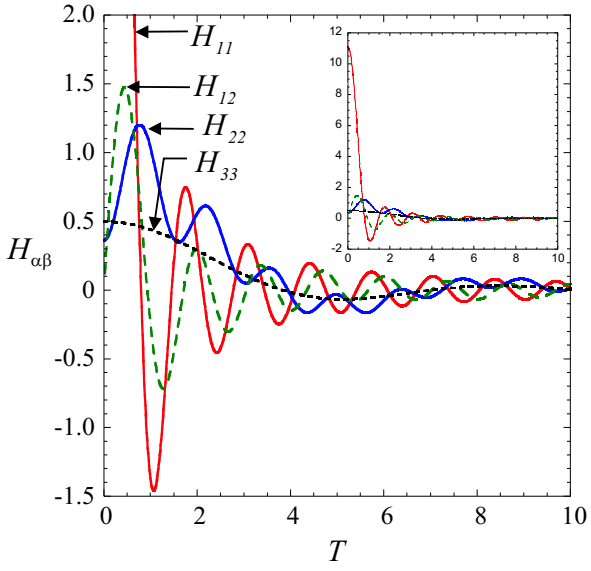

Figure 2 : Convolution kernels entering the spectral formulation for a graphite/epoxy material

from Eq. 7 and obtain the displacement solution entering the convolution relations Eq. 9-11. Finally, in order to simulate dynamic fracture problems involving the spontaneous initiation, propagation and arrest of a crack, a cohesive-based failure model must be introduced to relate the strength of the material along the fracture plane to the displacement and/or velocity discontinuities. Among the wide range of cohesive models that can be incorporated in the spectral scheme, we use hereafter a relatively simple rate-independent coupled cohesive failure model, which relates the normal and shear strengths along the fracture plane to the normal (δ_n) and tangential (δ_s) displacement discontinuities across the fracture plane as

$$\tau_{n,s}^{str} = \tau_{n,s}^{c}\left\langle 1 - \sqrt{\left(\frac{\delta_n}{\delta_n^c}\right)^2 + \left(\frac{\delta_s}{\delta_s^c}\right)^2}\right\rangle, \qquad (12)$$

where $\langle a\rangle = a$ if $a > 0$ and $\langle a\rangle = 0$ otherwise; τ_n^c and τ_s^c denote the intact tensile and shear strengths of the fracture plane, while δ_n^c and δ_s^c correspond to the critical values of the normal and shear crack opening displacements beyond which complete failure is achieved.

The numerical implementation of the spectral scheme for the transversely isotropic problem is similar to that used in the isotropic case by Morrissey and Geubelle (1997) and by Breitenfeld and Geubelle (1998). For completeness purpose, let us indicate that it involves the discretization of a period X of the fracture plane by N uniformly spaced grid points separated by X/N. A Fourier series representation of the displacements and

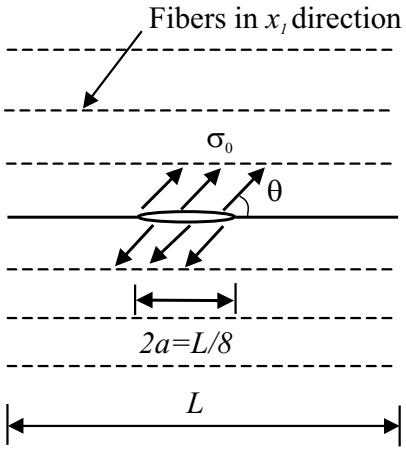

Figure 3 : Schematic of the stationary crack problem: finite size crack subjected to a sudden uniform mixed-mode loading in a unidirectional composite ($2a = 0.025\ m$, $L = 0.2\ m$, $\theta = 45^\circ$, $\sigma_0 = 18\ MPa$)

dynamic stress distribution is then introduced as

$$\left[u_j^{\pm}(x_1,t), f_j^{\pm}(x_1,t)\right] = \sum_{k=-N/2}^{N/2} \left[U_j^{\pm}(t), F_j^{\pm}(t)\right] \exp\left[2\pi i k x/X\right] \tag{13}$$

with the conversion between spectral and real domains performed efficiently through an FFT algorithm, using the N grid points as sampling points. The aforementioned time stepping scheme is explicit. The time step size is therefore dictated by the classical Courant stability condition.

3 Stationary cracks subjected to dynamic loading

The first numerical example investigates a non-propagating finite-sized crack embedded in a unidirectional 0° graphite/epoxy composite material and subjected to a sudden uniform mixed-mode loading (Fig. 3). The emphasis here is to show that the spectral scheme is able to capture accurately the complex wave interactions characterizing this problem and can be used to extract near-tip quantities such as stress intensity factors.

Let L denote the discretized portion of the fracture plane, and let $2a = L/8$ be the length of the pre-existing crack located at the center of the discretized domain, on which an uniform grid of 2048 elements is defined. The crack is prevented from extending by applying a very high strength in the uncracked region. In the cracked portion of the domain, the strength is equal to zero. The amount of mode mixity is denoted by angle θ, with $\theta = 0^\circ$ and 90° corresponding to pure tensile (mode-I) and pure shear (mode-II) loading, respectively. For this problem, angle θ is taken to be 45°. The initial crack is suddenly loaded with a uniform mixed-mode stress σ_o . The

Table 1 : Properties of the graphite/epoxy unidirectional composite

Elastic constants		Material properties	
c_{11}	82 *GPa*	E_1	80 *GPa*
c_{22}	11.1 *GPa*	$E_2 = E_3$	8.9 *GPa*
c_{12}	4.0 *GPa*	$\nu_{12} = \nu_{13}$	0.25
c_{23}	4.9 *GPa*	ν_{23}	0.43
c_{66}	3.6 *GPa*	$\mu_{12} = \mu_{13}$	3.6 *GPa*
ρ	1478 kg/m^3	μ_{23}	3.1 *GPa*

Table 2 : Types and arrival times of the elastic waves observed at a point A located at a distance $a/4$ ahead of the left crack tip (Fig. 4)

Indicators	Wave type	Originating crack tip	Arrival time $(c_s t/2a)$
A[1]	Dilatational wave	1	0.0262
A[2]	Shear wave	1	0.1250
A[3]	Dilatational wave	2	0.2356
A[4]	Shear wave	2	1.1252

transversely isotropic elastic constants and material properties for graphite/epoxy composite are given in Table 1 (Coker and Rosakis, 1998). The corresponding bulk wave speeds under plane strain conditions are $c_d^{(1)} = 7450\ m/s$, $c_d^{(2)} = 2740\ m/s$, and $c_s = 1560\ m/s$. The Rayleigh wave speed is $c_R = 1548\ m/s$.

Fig. 4 and 5 present the evolution of the normal ($\dot{u}_2$) and tangential ($\dot{u}_1$) velocities as a function of non-dimensional time $(c_s t/2a)$ at two points located at a distance $a/4$ ahead (point A) and behind (point B) the left crack tip, respectively. The square bracketed numbers in these figures indicate the arrival of various elastic waves originating from the crack-tips at points A and B, respectively. Tables 2 and 3 list the exact values of arrival time of the elastic waves at the points A and B, showing excellent agreement with the numerical values obtained in Fig. 4 and 5.

Turning now to the computation of near-tip quantities, the dynamic stress intensity factors for the unidirectional case can readily be extracted from the computed displacement discontinuities in the vicinity of the crack tips (Liu, Rosakis, Ellis and Stout, 1998; Wu, 1989) as

$$K_I(t) = \lim_{r\to 0} \frac{\gamma^{3/4}}{4b_{11}\sqrt{1+\omega}} \sqrt{\frac{\pi}{r}} \left[u_2^+(r,t) - u_2^-(r,t)\right], \tag{14}$$

$$K_{II}(t) = \lim_{r\to 0} \frac{\gamma^{1/4}}{4b_{11}\sqrt{1+\omega}} \sqrt{\frac{\pi}{r}} \left[u_1^+(r,t) - u_1^-(r,t)\right], \tag{15}$$

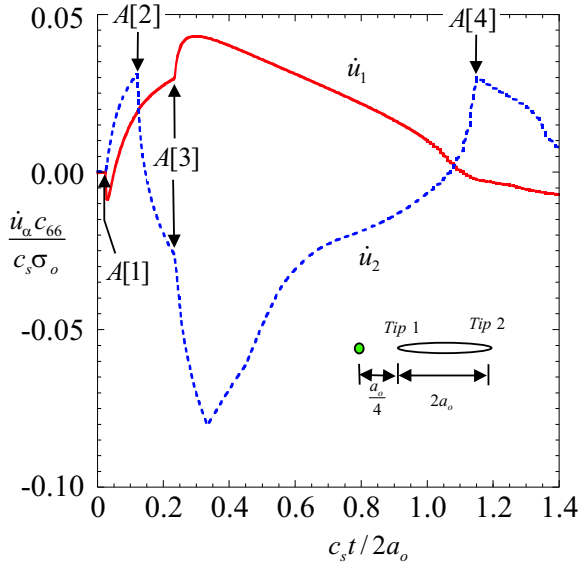

Figure 4 : Evolution of the velocities at a point A located ahead of the crack for a stationary crack under uniform sudden mixed-mode loading. The square bracketed numbers denote the time of arrival at point A of the elastic waves originating from the crack tips (see Table 2)

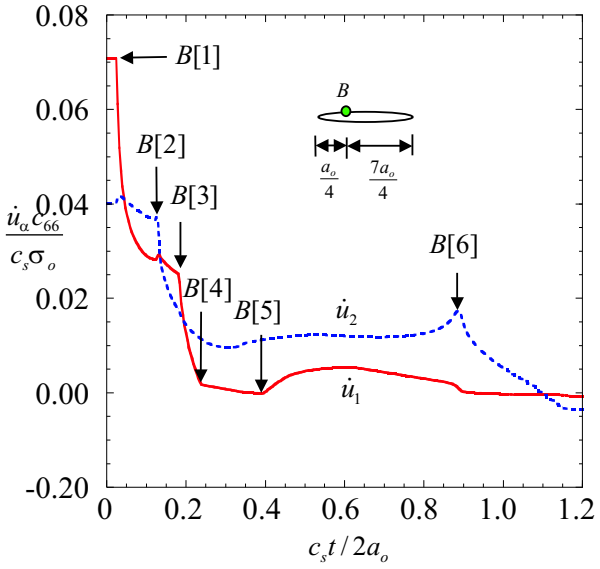

Figure 5 : Evolution of the velocities at a point B located ahead of the crack for a stationary crack under uniform sudden mixed-mode loading. The square bracketed numbers denote the time of arrival at point B of the elastic waves originating from the crack tips (see Table 3)

where r is a distance from the crack tip and b_{11}, γ and ω are defined as

$$b_{11} = \frac{c_{22}}{c_{11}c_{22} - c_{12}^2}, \quad \gamma = \frac{c_{22}}{c_{11}}, \quad \omega = \frac{2c_{12}c_{66} - c_{11}c_{22} + c_{12}^2}{2c_{66}\sqrt{c_{11}c_{22}}} > 1 \tag{16}$$

Fig. 6 illustrates the evolution of the dynamic stress intensity factors for the problem described in Fig. 3. The mode I and II dynamic stress intensity factors are normalized by their static values $K_I(\infty) = \sigma_0 \sin\theta\sqrt{\pi a}$, $K_{II}(\infty) = \sigma_0 \cos\theta\sqrt{\pi a}$: (Krenk, 1975).

As apparent in Fig. 6, the dynamic overshoot is more pronounced for the mode I singularity. The difference in rise time between $K_I(t)$ and $K_{II}(t)$ is also clearly visible: while the maximum value of $K_I(t)$ is achieved with the arrival of the Rayleigh wave emitted from the other crack tip, $K_{II}(t)$ reaches its maximum at the time of arrival of the dilatational wave. This result is in accordance with the conclusions reached by Rubio-Gonzalez and Mason (1999).

4 Subsonic and intersonic crack propagation

As indicated in the introductory section, observations of dynamic failure in unidirectional graphite/epoxy composites performed recently by Coker and Rosakis (1998) have yielded somewhat unexpected results. Under dynamic tensile (mode I) loading, subsonic crack motion (i.e., at speeds below the Rayleigh wave speed) is observed, and, unlike in the homogeneous case for which tensile cracks hardly exceed 0.4 to 0.5 c_R due to branching instabilities, mode I cracks in unidirectional composites can achieve propagation speeds approaching c_R . When the composite is subjected to dynamic shear (mode II) loading, cracks tend to enter the intersonic regime, for which the crack velocity v_c exceeds the shear wave speed c_s of the surrounding material, but remains below the dilatational wave speed $c_d^{(1)}$. This fracture response of unidirectional composites is reminiscent of recently observed intersonic crack mo-

Table 3 : Types and arrival times of the elastic waves observed at a point B located at a distance a/4 behind the left crack tip (Fig. 5)

Indicators	Wave type	Originating crack tip	Arrival time $(c_s t/2a)$
B[1]	Dilatational wave	1	0.0262
B[2]	Rayleigh wave	1	0.1263
B[3]	Dilatational wave	2	0.1832
B[4]	Dilatational wave (reflected at tip 1)	2	0.2356
B[5]	Dilatational wave (reflected at tip 2)	1	0.3926
B[6]	Rayleigh wave	2	0.8840

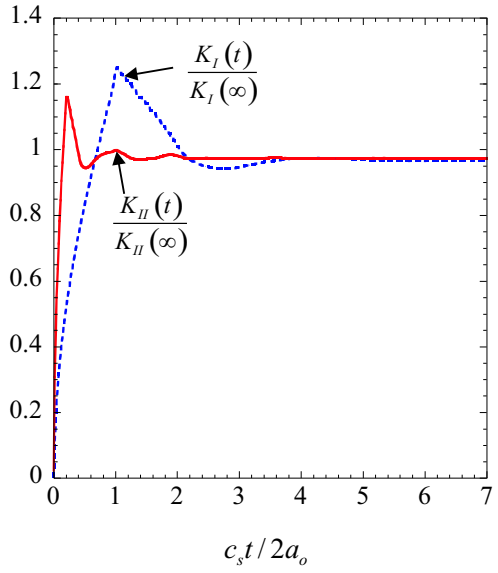

Figure 6 : Evolution of the dynamic stress intensity factors for a suddenly uniformly loaded mixed-mode stationary crack

Table 4 : The elastic wave speeds 0° and 90° graphite/epoxy composite

Wave speeds	Fibers parallel to x_1-axis	Wave speeds	Fibers parallel to x_3-axis
$c_d^{(1)}$	7450 m/s	$c_d^{(1)}$	2740 m/s
$c_d^{(2)}$	2740 m/s	$c_d^{(2)}$	2740 m/s
c_s	1560 m/s	c_s	1448 m/s
c_R (=0.99 c_s)	1548 m/s	c_R (=0.99 c_s)	1433 m/s

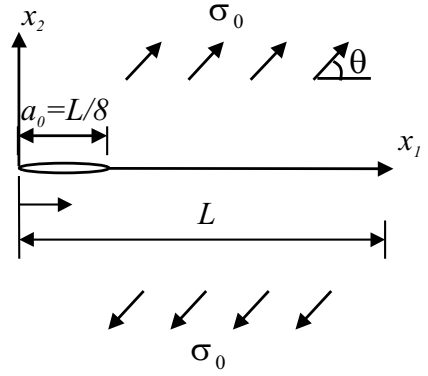

Figure 7 : Schematic of the dynamic crack propagation problem

tion in homogeneous isotropic specimens subjected to shear loading (Rosakis, Samudrala and Coker, 1999). However, unlike in the isotropic case where a weak plane has to be introduced ahead of the pre-crack to prevent the shear-loaded crack from kinking out of its original plane, weak planes exist naturally in unidirectional composites parallel to the fiber direction. Any deviation from planar crack motion is faced with a substantial energetic penalty associated with the fiber breakage and pullout processes. To investigate the intersonic motion of a crack in a unidirectional composite, Huang, Wang, Liu and Rosakis (1999) have presented an asymptotic analysis of the near-tip fields for a steadily propagating mode-II crack, showing the existence in the intersonic range of a critical crack tip velocity characterized by a non-vanishing energy release rate. The steady-state intersonic mode-II crack problem was also studied by Broberg (1999), who also determined the energy flow into the process region using the Barenbhalt cohesive failure model.

In a recent numerical analysis, Geubelle and Kubair (2000) have used the isotropic version of the spectral scheme to study various issues associated with the subsonic to intersonic transition in isotropic systems under pure mode II and mixed-mode conditions. Building on the success of this analysis, we show in this section how the spectral scheme developed above can be used to study accurately the subsonic and intersonic fracture of unidirectional graphite/epoxy composites and reproduce the experimental results of Coker and Rosakis. While we limit our investigation to the pure mode I and mode II loading cases, we study three material systems: the homogeneous 0° and 90° cases, and the bimaterial [0/90] problem (Fig. 1). The model dynamic fracture problem simulated hereafter is schematically shown in Fig. 7. It consists of a pre-stressed graphite/epoxy specimen subjected to uniform tensile ($\theta = 0^\circ$) or shear ($\theta = 90^\circ$) loading $\sigma_0 = 18\ MPa$. At time $t = 0$, a crack of initial length $a_0 = L/8$ (where $L = 0.2\ m$ denotes the discretized portion of the fracture plane) is introduced on the left side of the domain. Due to the dynamic stress concentration building up in its vicinity, the right crack tip starts to propagate along the x_1-axis, while the left crack tip is kept stationary. For simplicity we assume that the tensile and shear failure properties of the composite along the fracture plane are equal, both with regards to the strength values ($\tau_n^c = \tau_s^c = \tau^c = 36$ *MPa*) and the critical values of the crack opening displacements ($\delta_n^c = \delta_s^c = \delta^c = 26.3\ \mu m$) entering the cohesive failure model described in Eq. 12. 2048 equally spaced grid points are used to discretize the fracture plane, and the time step is chosen as $c_s \Delta t = 0.1 \Delta x$, where Δx denotes the grid point spacing. In all the simulations of spontaneous crack propagation, special care was taken to capture with cohesive failure zone with sufficient accuracy (typically, with at least 10 sampling points). The elastic wave speeds for the graphite/epoxy composite are listed in Table 4 for the two fiber orientations considered here.

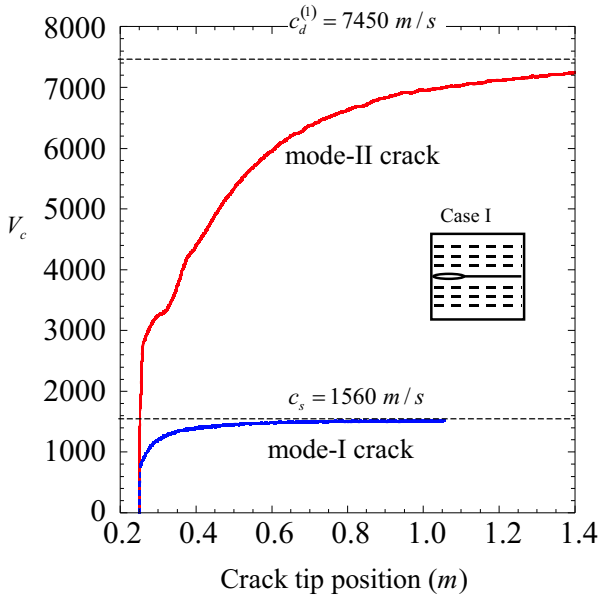

Figure 8 : Crack tip speed (V_c) as a function of crack tip position for mode-I and mode-II cracks in case I: unidirectional 0° case

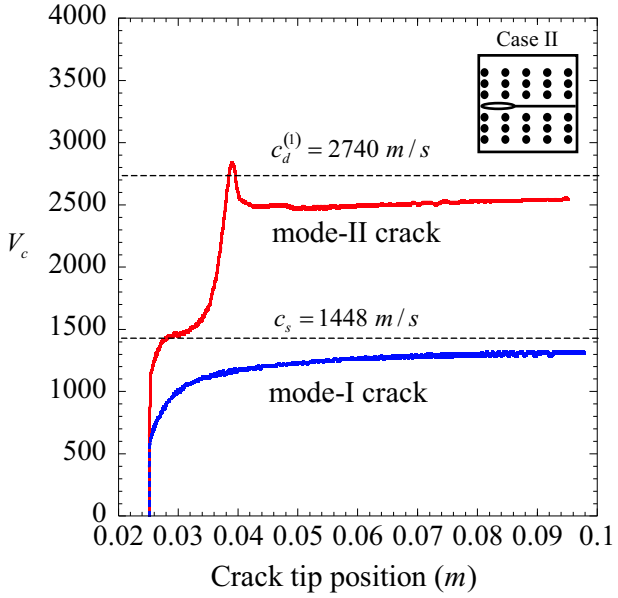

Figure 9 : Crack tip speed (V_c) as a function of crack tip position for mode-I and mode-II cracks in case II: unidirectional 90° case

Fig. 8 and 9 illustrate the evolution of the crack tip speed as a function of crack tip position for the two unidirectional composite specimens subjected to both mode-I and mode-II loading. The results relative to the 0° unidirectional composite (Fig. 8) are directly relevant to the experiments performed by Coker and Rosakis (1998), although the impact loading used in their experiments is quite different from the uniform preloading used in our model dynamic fracture problem. As was the case in their experiments (see Fig. 19 of Coker and Rosakis (1998)), the mode I loaded crack remains subsonic and quickly approaches the Rayleigh wave speed. In the mode II case, the crack quickly exceeds the shear wave speed and becomes intersonic. In our particular setting, for which energy is continuously provided to the crack tip region, the crack keeps accelerating and asymptotically approaches the dilatational wave speed $c_d^{(1)}$

A similar behavior is observed in the unidirectional 90° case (Fig. 9). It should be noted that, in this case II, the in-plane crack problem on x_1-x_2 plane is basically a 2D homogeneous, isotropic problem, and, as mentioned earlier, a weak plane would need to be introduced in practice ahead of the pre-crack to maintain planar crack motion in the mode II case. In the mode I situation, branching instabilities are likely to occur, which would prevent the crack from reaching such high subsonic velocities, unless, once again, a weaker plane is introduced ahead of the crack as was shown in the isotropic case by Washabaugh and Knauss (1994).

Results for the cross-ply composite (case III) are presented in

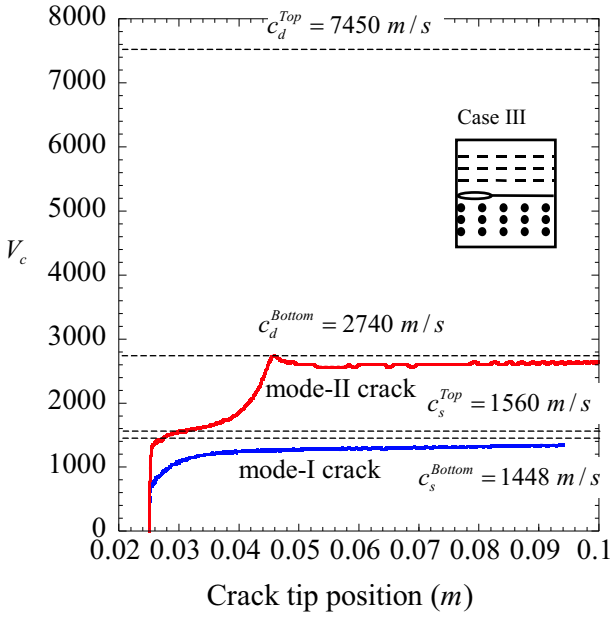

Figure 10 : Crack tip speed (V_c) as a function of crack tip position for mode-I and mode-II cracks in bimaterial case III

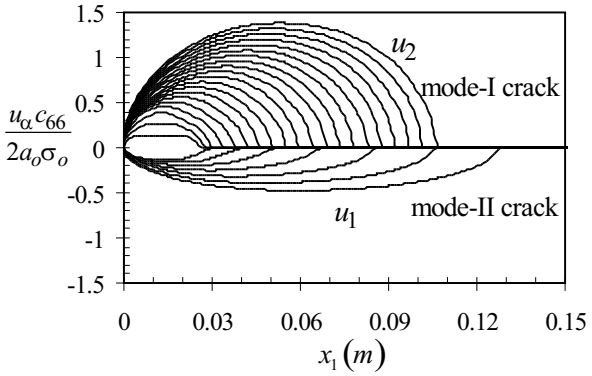

Figure 11 : Snapshots of normalized displacement of dynamically propagating mode-I and mode-II cracks in case I: 0° unidirectional graphite/epoxy

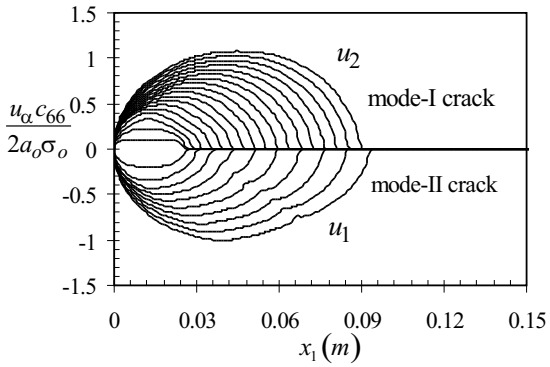

Figure 12 : Snapshots of normalized displacement of dynamically propagating mode-I and mode-II cracks in case II: 90° unidirectional graphite/epoxy

Fig. 10. Interestingly, results indicate that the maximum delamination speeds under mode-I and mode-II loading are respectively bounded by the shear and dilatational wave speeds of the more (in-plane) compliant (bottom) material. This result is quite different from that obtained for a Homalite/Aluminum isotropic problem (Breitenfeld and Geubelle, 1998), for which the maximum crack velocity was shown to be the Rayleigh wave speed of the stiffer material. Note that, in that particular case, the Rayleigh wave speed of the stiffer material (Aluminum) exceeded the dilatational wave speed of the more compliant one (Homalite) due to the very strong material mismatch between the two components.

To further illustrate the characteristics of subsonic mode I and intersonic (mode II) crack propagation, Fig. 11 and 12 present the evolution of the main displacement components (normal displacement u_2 in the mode I case, and tangential displacement u_1 in the mode II case) for the 0° and 90° unidirectional problems, respectively. The various curves are separated by the same time interval of 500 time steps. Taking advantage of mirror (anti)symmetry, both the modes I and II are shown on the same figures. The two figures clearly illustrate the very rapid motion of the mode II crack in the 0° unidirectional case. The Rayleigh wave surface perturbation characteristic of subsonic-to-intersonic transition in the isotropic case (Geubelle and Kubair, 2000) is clearly visible in the mode II 90° case shown in Fig. 12.

Finally, the evolution of the displacements of the top and bottom crack surface obtained during the dynamic delamination process in bimaterial system is presented in Fig. 13 (mode I) and 14 (mode II). Note the strong asymmetry present in the mode II case between the two components. In the mode I loading case, the top and bottom composite materials offer relatively similar resistance to transverse motion.

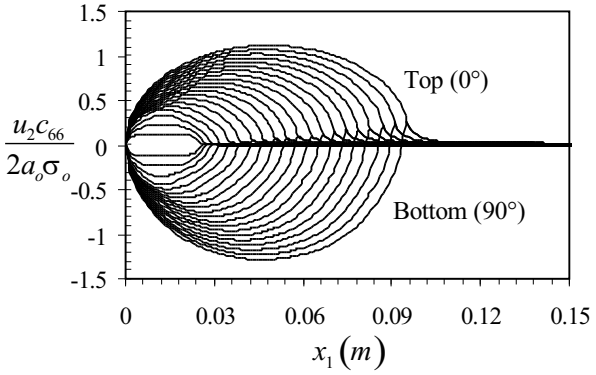

Figure 13 : Snapshots of normalized vertical displacement of dynamically propagating mode-I crack in bimaterial case III

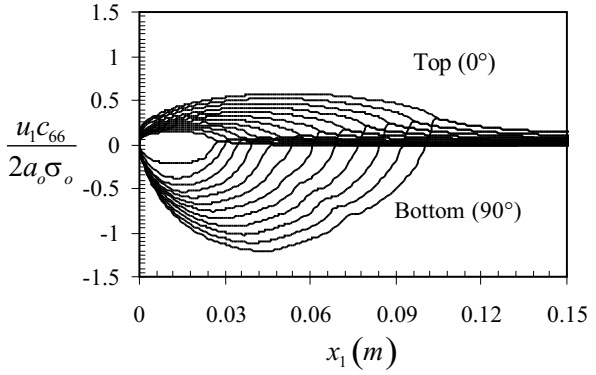

Figure 14 : Snapshots of normalized horizontal displacement of dynamically propagating mode-II crack in bimaterial case III

5 Conclusions

A spectral scheme has been developed to simulate dynamic fracture in a class of unidirectional and cross-ply fiber-reinforced composites. The method is based on the spectral representation of the transversely isotropic elastodynamic relations between the traction stresses along the fracture plane and the resulting displacements. It was demonstrated through numerical examples that the spectral method not only captured precisely the complex wave interactions associated with dynamic fracture of fiber-reinforced composites, but also the subsonic and intersonic crack propagation for mode-I and mode-II cracks. Bimaterial effect on the simulation of dynamic fracture in fiber-reinforced composites was also investigated, showing that the maximum spontaneous debonding speeds under mode I and II in-plane loading conditions are bounded by the lower shear wave and dilatational wave speed of the bimaterial system.

Acknowledgement: This work has been supported by the ASCI Center for the Simulation of Advanced Rockets funded by the U.S. Department of Energy through the University of California under subcontract B341494.

References

Abrate, S. (1998): *Impact of Composite Structures*. Cambridge University Press, NY.

Breitenfeld, M. S.; Geubelle, P. H. (1998): Numerical analysis of dynamic debonding under 2D in-plane and 3D loading. *Int. J. Fracture*, vol. 93, pp. 13–38.

Broberg, K. B. (1999): Intersonic crack propagation in an orthotropic material. *Int. J. Fracture*, vol. 99, pp. 1–11.

Chai, H.; Knauss, W. G.; Babcok, C. D. (1983): Observation of damage growth in compressively loaded laminates. *Experimental Mechanics*, vol. 23, pp. 329–337.

Coker, D.; Rosakis, A. J. (1998): Experimental observations of intersonic crack growth in asymmetrically loaded unidirectional composites plates. In *GALCIT SM Report 98-16*. Caltech. To appear in Philosophical Magazine A (2000).

Geubelle, P. H.; Baylor, J. (1998): Impact-induced delamination of composites: a 2D simulation. *Composites B*, vol. 29B, pp. 589–602.

Geubelle, P. H.; Breitenfeld, M. S. (1997): Numerical analysis of dynamic debonding under anti-plane shear loading. *Int. J. Fracture*, vol. 85, pp. 265–282.

Geubelle, P. H.; Kubair, D. (2000): Intersonic crack propagation in homogeneous media: Numerical analysis. *J. Mech. Physics Solids to appear*.

Geubelle, P. H.; Rice, J. R. (1995): A spectral method for 3D elastodynamic fracture problems. *J. Mech. Phys. Solids*, vol. 43, no. 11, pp. 1791–1824.

Huang, Y.; Wang, W.; Liu, C.; Rosakis, A. J. (1999): Analysis of intersonic crack growth in unidirectional fiber-reinforced composites. *J. Mech. Physics Solids*, vol. 47, pp. 1893–1916.

Krenk, S. (1975): The stress distribution in an infinite anisotropic plate with co-linear cracks. *Int. J. Solids Structures*, vol. 11, pp. 449–460.

Lambros, J. M.; Rosakis, A. J. (1997a): An experimental study of the dynamic delamination of thick reinforced polymeric matrix composite laminates. *Experimental Mechanics*, vol. 37, no. 3, pp. 360–366.

Lambros, J. M.; Rosakis, A. J. (1997b): Dynamic crack initiation and growth in thick unidirectional graphite/epoxy plates. *Composites Science and Technology*, vol. 57, no. 1, pp. 55–65.

Liu, C.; Rosakis, A. J.; Ellis, R. W.; Stout, M. G. (1998): A study of the fracture behavior of unidirectional fiber-reinforced composites using Coherent Gradient Sensing (CGS) interferometry. *Int. J. Fracture*, vol. 90, pp. 355–382.

Morrissey, J. W.; Geubelle, P. H. (1997): A numerical scheme for mode III dynamic fracture problems. *Int. J. Numer. Methods Eng.*, vol. 40, pp. 1181–1196.

Rosakis, A. J.; Samudrala, O.; Coker, D. (1999): Cracks faster than the shear wave speed. *Science*, vol. 284, pp. 1337–1340.

Rubio-Gonzalez, C.; Mason, J. J. (1999): Response of finite cracks in orthotropic materials due to concentrated impact shear loads. *J. Appl. Mech.*, vol. 66, pp. 485–491.

Washabaugh, P. D.; Knauss, W. G. (1994): A reconciliation of dynamic crack velocity and rayleigh wave speed in isotropic brittle solids. *Int. J. Fracture*, vol. 65, no. 2, pp. 97–114.

Wu, K. (1989): On the crack-tip fields of a dynamically propagating crack in an anisotropic elastic solid. *Int. J. Fracture*, vol. 41, pp. 253–266.

Appendix A:

In case that the fiber axis coincides with the x_3-axis (see Fig. 1b), the stress-strain relationship is given by

$$\begin{Bmatrix} \sigma_{11} \\ \sigma_{22} \\ \sigma_{33} \\ \sigma_{23} \\ \sigma_{13} \\ \sigma_{12} \end{Bmatrix} = \begin{bmatrix} c_{11} & c_{12} & c_{13} & 0 & 0 & 0 \\ c_{12} & c_{11} & c_{13} & 0 & 0 & 0 \\ c_{13} & c_{13} & c_{33} & 0 & 0 & 0 \\ 0 & 0 & 0 & c_{44} & 0 & 0 \\ 0 & 0 & 0 & 0 & c_{44} & 0 \\ 0 & 0 & 0 & 0 & 0 & c_{66} \end{bmatrix} \begin{Bmatrix} \varepsilon_{11} \\ \varepsilon_{22} \\ \varepsilon_{33} \\ 2\varepsilon_{23} \\ 2\varepsilon_{13} \\ 2\varepsilon_{12} \end{Bmatrix} \tag{17}$$

where $c_{66} = (c_{11} - c_{12})/2$. The equations of motion are given by

$$c_{11}\frac{\partial^2 u_1}{\partial x_1^2} + c_{66}\frac{\partial^2 u_1}{\partial x_2^2} + (c_{12} + c_{66})\frac{\partial^2 u_2}{\partial x_1 \partial x_2} = \rho\frac{\partial^2 u_1}{\partial t^2}, \tag{18}$$

$$c_{66}\frac{\partial^2 u_2}{\partial x_1^2} + c_{11}\frac{\partial^2 u_2}{\partial x_2^2} + (c_{12} + c_{66})\frac{\partial^2 u_1}{\partial x_1 \partial x_2} = \rho\frac{\partial^2 u_2}{\partial t^2}, \tag{19}$$

for in-plane motion and

$$c_{44}\frac{\partial^2 u_3}{\partial x_1^2} + c_{44}\frac{\partial^2 u_3}{\partial x_2^2} = \rho\frac{\partial^2 u_3}{\partial t^2} \tag{20}$$

for out-of-plane motion.

Appendix B:

Let $T_\alpha(t;q)$ and $U_\alpha(t;q)$ denote the q^{th}-mode Fourier coefficients of the traction stresses acting on the fracture plane and the corresponding displacements, respectively, as in

$$\sigma_{2j}(x_1, 0, t) = \tau_j(x_1, t) = T_j(t;q)e^{iqx_1}, \tag{21}$$

$$u_j(x_1, 0^\pm, t) = u_j^\pm(x_1, t) = U_j^\pm(t;q)e^{iqx1}. \tag{22}$$

In case that the fiber axis coincides with the x_1-axis (see Fig. 1a), the relations between Fourier coefficients of the traction stresses along the fracture plane and those of the resulting displacements in the Laplace domain are given by

$$\hat{T}_1(p;q) = \mp c_{66}^\pm |q| \left[\frac{-W^\pm c_d^{(1)\pm} c_d^{(2)\pm} \alpha_d^\pm}{|q|\left(c_d^{(1)\pm} c_d^{(2)\pm} \alpha_d^\pm + c_s^{\pm 2} \alpha_s^\pm\right)}\right] \hat{U}_1^\pm(p;q)$$
$$+ ic_{66}^\pm q \left[2 - \frac{c_d^{(1)\pm} c_d^{(2)\pm} \alpha_d^\pm + c_s^{\pm 2} \alpha_s^\pm \left(2 + c_{12}^\pm / c_{66}^\pm\right)}{|q|\left(c_d^{(1)\pm} c_d^{(2)\pm} \alpha_d^\pm + c_s^{\pm 2} \alpha_s^\pm\right)}\right]$$
$$\times \hat{U}_2^\pm(p;q) \tag{23}$$

$$\hat{T}_2(p;q) = \mp c_{66}^\pm |q| \left[\frac{-W^\pm c_d^{(2)\pm 2} \alpha_d^\pm}{|q|\left(c_d^{(1)\pm} c_d^{(2)\pm} \alpha_d^\pm + c_s^{\pm 2} \alpha_s^\pm\right)}\right] \hat{U}_2^\pm(p;q)$$
$$- ic_{66}^\pm q \left[2 - \frac{c_d^{(1)\pm} c_d^{(2)\pm} \alpha_d^\pm + c_s^{\pm 2} \alpha_s^\pm \left(2 + c_{12}^\pm / c_{66}^\pm\right)}{|q|\left(c_d^{(1)\pm} c_d^{(2)\pm} \alpha_d^\pm + c_s^{\pm 2} \alpha_s^\pm\right)}\right]$$
$$\times \hat{U}_1^\pm(p;q) \tag{24}$$

$$\hat{T}_3(p;q) = \mp \frac{c_{66}^\pm}{\beta^\pm} |q| \alpha_s^\pm \hat{U}_3^\pm(p;q) \tag{25}$$

where $\hat{f}(p)$ denotes the Laplace transform of $f(t)$ and

$$\alpha_d = \sqrt{1 + \frac{p^2}{q^2 c_d^{(1)2}}}, \tag{26}$$

$$\alpha_s = \sqrt{1 + \frac{p^2}{q^2 c_s^2}}, \tag{27}$$

$$W = \frac{|q|}{c_s c_d^{(2)}} \times \sqrt{\left(c_d^{(2)}\sqrt{c_d^{(2)2} + c_s^2 s^2} + \alpha_s c_s^2\right)^2 - \left(c_s^2 + \frac{c_{12}}{\rho}\right)^2} \tag{28}$$

We can extract the instantaneous responses as

$$\left[\hat{T}_1\right]_{inst} = \mp \frac{c_{66}^\pm}{c_s^\pm} p\hat{U}_1^\pm(p;q) \tag{29}$$

$$\left[\hat{T}_2\right]_{inst} = \mp \frac{c_d^{(2)\pm}}{c_s^{\pm 2}} c_{66}^\pm p\hat{U}_2^\pm(p;q) \tag{30}$$

$$\left[\hat{T}_3\right]_{inst} = \mp \frac{c_{66}^\pm}{\beta^\pm c_s^\pm} p\hat{U}_3^\pm(p;q) \tag{31}$$

and rewrite Eq. 23-25 as

$$\hat{T}_1(p;q) = \mp \frac{c_{66}^\pm}{c_s^\pm} p\hat{U}_1^\pm(p;q) \mp c_{66}^\pm |q|$$
$$\times \left[\frac{-W^\pm c_d^{(1)\pm} c_d^{(2)\pm} \alpha_d^\pm}{|q|\left(c_d^{(1)\pm} c_d^{(2)\pm} \alpha_d^\pm + c_s^{\pm 2} \alpha_s^\pm\right)} - \frac{p}{|q| c_s^\pm}\right] \hat{U}_1^\pm(p;q)$$
$$+ ic_{66}^\pm q \left[2 - \frac{c_d^{(1)\pm} c_d^{(2)\pm} \alpha_d^\pm + c_s^{\pm 2} \alpha_s^\pm \left(2 + c_{12}^\pm / c_{66}^\pm\right)}{|q|\left(c_d^{(1)\pm} c_d^{(2)\pm} \alpha_d^\pm + c_s^{\pm 2} \alpha_s^\pm\right)}\right]$$
$$\times \hat{U}_2^\pm(p;q) \tag{32}$$

$$\hat{T}_2(p;q) = \mp \frac{c_d^{(2)\pm}}{c_s^{\pm 2}} c_{66}^\pm p\hat{U}_2^\pm(p;q) \mp c_{66}^\pm |q|$$
$$\times \left[\frac{-W^\pm c_d^{(2)\pm 2} \alpha_d^\pm}{|q|\left(c_d^{(1)\pm} c_d^{(2)\pm} \alpha_d^\pm + c_s^{\pm 2} \alpha_s^\pm\right)} - \frac{c_d^{(2)\pm}}{c_s^\pm} \frac{p}{|q| c_s^\pm}\right] \hat{U}_2^\pm(p;q)$$
$$- ic_{66}^\pm q \left[2 - \frac{c_d^{(1)\pm} c_d^{(2)\pm} \alpha_d^\pm + c_s^{\pm 2} \alpha_s^\pm \left(2 + c_{12}^\pm / c_{66}^\pm\right)}{|q|\left(c_d^{(1)\pm} c_d^{(2)\pm} \alpha_d^\pm + c_s^{\pm 2} \alpha_s^\pm\right)}\right]$$
$$\times \hat{U}_1^\pm(p;q) \tag{33}$$

$$\hat{T}_3(p;q) = \mp \frac{c_{66}^\pm}{\beta^\pm} |q| \left(\alpha_s^\pm - \frac{p}{|q| c_s^\pm}\right) \hat{U}_3^\pm(p;q)$$
$$\mp \frac{c_{66}^\pm}{\beta^\pm c_s^\pm} p\hat{U}_3^\pm(p;q) \tag{34}$$

Back in the space-time domain, the 2D elastodynamic relations between the traction components of the stress $\tau_i(x_1, t)$ acting on the fracture plane and the resulting displacements $u_i^\pm(x_1, t)$ take the form.

$$\tau_i(x_1, t) = \tau_i^0(x_1, t) \mp V_{ik}^\pm \frac{\partial u_k^\pm(x_1, t)}{\partial t} + f_i^\pm(x_1, t) \tag{35}$$

where V_{ij} is given in Eq. 8.

Appendix C:

The convolution kernels $H_{\alpha\beta}$ for in-plane motion entering Eq. 9-11, in the 0° case (see Fig. 1a), are defined as

$$H_{11}(T) = L^{-1}\left\{\left[\sqrt{s^2+\eta^{(1)^2}} \times\sqrt{\left(\eta^{(2)}\sqrt{s^2+\eta^{(1)^2}}+\sqrt{1+s^2}\right)^2-\left(1+\eta^{(3)^2}\right)^2}\right] \Big/\left[\eta^{(2)}\sqrt{s^2+\eta^{(1)^2}}+\sqrt{1+s^2}\right]-s\right\} \quad (36)$$

$$H_{12}(T) = L^{-1}\left\{\left[-\eta^{(2)}\sqrt{s^2+\eta^{(1)^2}}-\sqrt{1+s^2}\left(2+\eta^{(3)^2}\right)\right] \Big/\left[\eta^{(2)}\sqrt{s^2+\eta^{(1)^2}}+\sqrt{1+s^2}\right]+\frac{2+\eta^{(2)}+\eta^{(3)^2}}{1+\eta^{(2)}}\right\} \quad (37)$$

$$H_{22}(T) = L^{-1}\left\{\left[\eta^{(2)}\sqrt{1+s^2} \times\sqrt{\left(\eta^{(2)}\sqrt{s^2+\eta^{(1)^2}}+\sqrt{1+s^2}\right)^2-\left(1+\eta^{(3)^2}\right)^2}\right] \Big/\left[\eta^{(2)}\sqrt{s^2+\eta^{(1)^2}}+\sqrt{1+s^2}\right]-\eta^{(2)}s\right\} \quad (38)$$

where $s = p/c_s|q|$. The convolution kernels are readily inverted back to the time domain using conventional numerical Laplace inversion algorithms.

Appendix D:

The spectral formulation corresponding to the 90° case (see Fig. 1b) is summarized hereafter. The 2D elastodynamic relations between the traction components of the stress $\tau_i(x_1,t)$ acting on the fracture plane and the resulting displacements $u_i^{\pm}(x_1,t)$, in the space-time domain, take the form

$$\tau_i(x_1,t) = \tau_i^0(x_1,t) \mp V_{ik}^{\pm}\frac{\partial u_k^{\pm}(x_1,t)}{\partial t} + f_i^{\pm}(x_1,t), \quad (39)$$

where $V_{11} = c_{66}/c_s$, $V_{22} = c_d^{(2)}c_{66}/c_s^2$, $V_{33} = c_{66}/c_s$.
The associated Fourier coefficients $F_i(t;q)$ are given by

$$F_1^{\pm}(t;q) = \pm c_{66}^{\pm}|q|\int_0^t H_{11}\left(|q|c_s^{\pm}t'\right)U_1^{\pm}\left(t-t';q\right)|q|c_s^{\pm}dt' + ic_{66}^{\pm}|q|\int_0^t H_{12}\left(|q|c_s^{\pm}t'\right)U_2^{\pm}\left(t-t';q\right)|q|c_s^{\pm}dt' + ic_{66}^{\pm}|q|\left(2-\eta^{(2)\pm}\right)U_2^{\pm}(t;q) \quad (40)$$

$$F_2^{\pm}(t;q) = \mp c_{66}^{\pm}|q|\int_0^t H_{22}\left(|q|c_s^{\pm}t'\right)U_2^{\pm}\left(t-t';q\right)|q|c_s^{\pm}dt' - ic_{66}^{\pm}|q|\int_0^t H_{12}\left(|q|c_s^{\pm}t'\right)U_1^{\pm}\left(t-t';q\right)|q|c_s^{\pm}dt' - ic_{66}^{\pm}|q|\left(2-\eta^{(2)\pm}\right)U_1^{\pm}(t;q) \quad (41)$$

$$F_3^{\pm}(t;q) = \mp c_{44}^{\pm}|q|\int_0^t H_{33}\left(|q|c_s^{\pm}t'\right)U_3^{\pm}(t-t';q)|q|c_s^{\pm}dt' \quad (42)$$

The convolution kernels corresponding to the 90° case are identical to those in the isotropic case. See the details in Geubelle and Breitenfeld (1997) and Breitenfeld and Geubelle (1998).